Volume 2
Number 6
November 2025
Pages 1495–1930

RSC Applied Interfaces

rsc.li/RSCApplInter

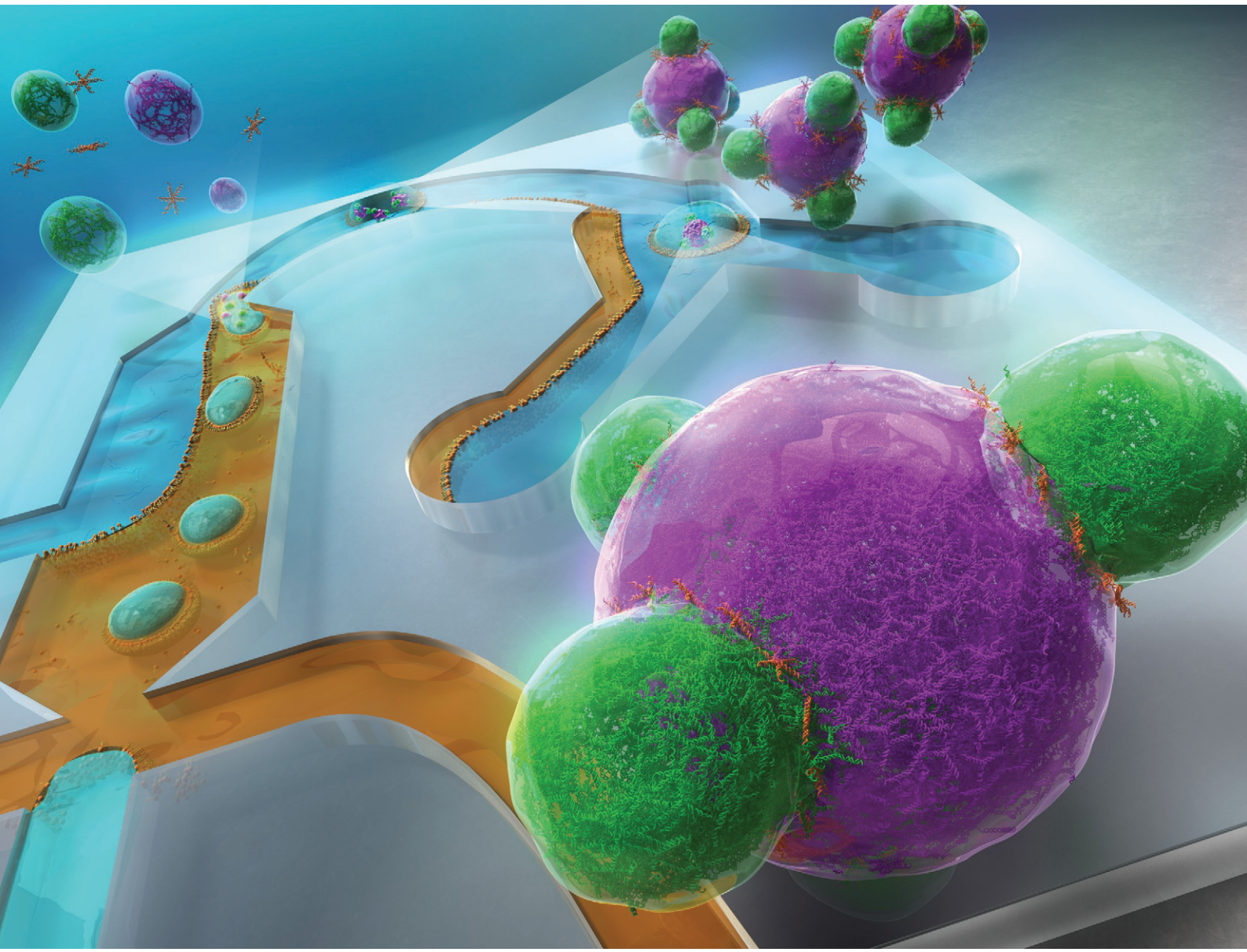

ISSN 2755-3701

ROYAL SOCIETY OF CHEMISTRY

PAPER
Hiroaki Suzuki *et al.*
Formation dynamics of patchy/Janus DNA condensates in monodisperse giant vesicles generated using microfluidics

RSC Applied Interfaces

ROYAL SOCIETY OF CHEMISTRY

PAPER

View Article Online
View Journal | View Issue

Cite this: *RSC Appl. Interfaces*, 2025, **2**, 1599

Formation dynamics of patchy/Janus DNA condensates in monodisperse giant vesicles generated using microfluidics

Ryotaro Yoneyama,[a] Ryota Ushiyama,[a] Tomoya Maruyama,[bd] Reiko Sato,[a] Mamiko Tsugane,[a] Masahiro Takinoue [bcd] and Hiroaki Suzuki *[a]

Received 9th May 2025,
Accepted 15th August 2025

DOI: 10.1039/d5lf00131e

rsc.li/RSCApplInter

Herein, we demonstrate the one-step formation of uniform patchy or Janus-type DNA condensates within monodisperse giant vesicles. This process was achieved by encapsulating DNA building blocks in monodisperse giant vesicles fabricated using a microfluidic device and then subjecting them to gradual concentration by shrinking the vesicles using osmotic action. The concentration of the linker DNA motif, which connects two immiscible condensates with orthogonal DNA nanostructures, was identified as a crucial parameter determining the morphology of patchy/Janus DNA condensates. Furthermore, the formation of condensates within uniformly sized giant vesicles allowed the production of patchy DNA condensates with a consistent morphology. Our approach is expected to offer a promising method for homogeneous production of artificial cells with complex functionalities.

Introduction

Janus and patchy particles, which are colloidal particles with more than a single type of surface chemistry or composition, have been extensively studied in the field of material science.[1–6] Unlike ordinal particles with isotropic surface properties, Janus and patchy particles exhibit asymmetrically distributed functions for use in various applications such as solid surfactants, microprobes, sensors, and self-propelling materials. One way to create such particles is to partially modify the surface of silica or polymer particles,[7,8] but more complicated and highly controlled structures can be obtained using polymerization or gelation after combining different types of precursors in liquid forms adjacent to each other.[9–12]

Among the various hydrogel materials, DNA condensates (DNA droplets and hydrogels) have been intensively studied as new smart materials, whose physical properties and environmental responses can be programmed through sequence design and molecular modifications.[13–17] In particular, DNA nanostar structures with multiple arms have been widely used as building blocks for DNA condensates offering facile and sophisticated modulation of physical properties (*e.g.*, fluidity, viscoelasticity, and interfacial tension) and functionalities. Such modulation can be achieved by adjusting various parameters in the structural design, such as the length and valency of the multivalent arms, their structural flexibility, and the GC content of the sticky ends (SEs) located at the tips of the arms.[18–23] Unlike dispersed nanostructures, such as DNA origami, the typical condensate size is meso- to microscopic; therefore, its state changes can be readily observed with ordinary apparatus such as optical microscopes and spectrometers. DNA condensates are expected to be applied not only to basic research on DNA structures but also to sensors,[24–28] enrichment/chemical-reaction platforms,[29–33] and the construction of artificial cells.[17,28,34–37]

Structures composed of multiple types of DNA condensates are expected to exhibit more complex structures and functions. In particular, nanostar motifs that form DNA condensates can be selectively controlled by designing SE sequences. Thus, providing orthogonality among multiple types of DNA nanostars and allowing different condensates to coexist in the same environment are possible.[21,38] Additionally, by designing and adding DNA structures having different SEs to link orthogonal condensates, controlling the coalescence and phase separation of orthogonal DNA condensates is possible.[21,39–41] Furthermore, these changes are shown to be triggered by external environmental factors.[35] Recently, Takinoue's group constructed a DNA hydrogel system in which the linker nanostar is decomposed

[a] *Department of Precision Mechanics, Graduate School of Science and Engineering, Chuo University, 1-13-27 Kasuga, Bunkyo-ku, Tokyo, 112-8551, Japan. E-mail: yoneyama@nano.mech.chuo-u.ac.jp, suzuki@mech.chuo-u.ac.jp*
[b] *Department of Life Science and Technology, Institute of Science Tokyo, 4259 Nagatsuda-cho, Midori-ku, Yokohama, Kanagawa 226-8501, Japan*
[c] *Department of Computer Science, Institute of Science Tokyo, 4259 Nagatsuda-cho, Midori-ku, Yokohama, Kanagawa 226-8501, Japan*
[d] *Research Center for Autonomous Systems Materialogy (ASMat), Institute of Integrated Reseach, Institute of Science Tokyo, 4259 Nagatsuda-cho, Yokohama, Kanagawa 226-8501, Japan*

by a strand displacement reaction and showed that mixed orthogonal DNA condensates underwent phase separation depending on the presence of a specific short RNA.[42,43] This system displays molecular binding as a macroscopic structural change and can be used to detect target nucleic acids.

To construct artificial cells that mimic the hierarchical structures of living cells, we established a system to control the generation of DNA condensates in uniform giant vesicles (GVs)[44] produced using microfluidics.[45,46] By modulating the vesicle volume through osmotic action, the concentration of the molecules contained within can be continuously altered. Because the formation of DNA condensates is dependent on the concentrations of DNA nanostructures and salts, we succeeded in dynamically controlling the formation/dissolution of DNA condensates without thermal annealing, which has been mainly used to promote the slow binding of SEs to form uniform condensates. In this study, we used a monodisperse GV-based system to examine the conditions required for generating uniform patchy and Janus DNA condensates in a controlled artificial cell-like environment.

Experimental

Oligonucleotide preparation

The oligonucleotides with oligonucleotide purification cartridge-grade purification were custom-ordered and purchased from Eurofins Genomics (Tokyo, Japan). Fluorophore-labeled oligonucleotides were purified using high-performance liquid chromatography grade. Sequences of the oligonucleotides and fluorophore-labeled oligonucleotides are provided in Table S1. These oligonucleotides were designed to form three-arm Y-shaped nanostructures (Y-motifs) with 6-nucleotide (nt) palindromic SEs. Two types of Y-motifs with mutually orthogonal SEs, referred to as Y_A and Y_B, were prepared. Additionally, a DNA nanostructure with six arms, having three SEs of each Y_A and Y_B, respectively (termed the S-motif), was prepared. The oligonucleotides were dissolved in Milli-Q water at 100 μM concentration as stock solutions and stored at −20 °C until use.

Preparation of DNA solution

In this study, we generated DNA condensates within GVs produced in a microfluidic device by reducing the GV volume to one-fifth through osmotic shrinkage, thereby concentrating the encapsulated oligonucleotides and salt, as we demonstrated previously.[44] Consequently, for the bulk DNA condensate formation experiments corresponding to these conditions, we used five times the concentration of all components encapsulated in the GVs. Specifically, the following DNA solution compositions were used (see Table S2 for details): the former for the bulk experiments and the latter for the initial concentration encapsulated in the GVs. Two sets of single-stranded DNA (ssDNA) comprising Y_A-motif and Y_B-motif, each composed of three ssDNA strands, were mixed at final concentrations of 5 or 1 μM each. A set of ssDNA forming a linker motif (S-motif), composed of six ssDNA strands, were mixed at either 0 μM, 0.05 or 0.5 μM each for bulk experiments, and 0 μM, 0.01 or 0.1 μM each for the *in vesicle* experiments. For fluorescent labeling, 10 mol% Y_{A2} or Y_{B2} was replaced with the corresponding fluorescently (cyanine 5 (Cy5) or 6-carboxyfluorescein (FAM)) labeled variants. Additionally, sucrose and dextran cascade blue (MW 10 000) were added at final concentrations of 500 or 100 mM and 100 or 20 μg mL^{-1}, respectively. After vortexing the mixture for 5 s, NaCl and Tris-HCl (pH 8.0) were added to final concentrations of 175 or 35 mM and 20 or 4 mM, respectively, followed by another round of vortexing.

Microscope observation of DNA condensates in bulk

To prevent DNA adsorption by wetting the glass substrate, we passivated the cover glass with polyvinyl alcohol (PVA, 87% hydrolyzed). Specifically, 80 μL of 2.5%w/v PVA aqueous solution was applied to the coverglass (25 mm × 25 mm, thickness 0.17 mm, Matsunami Glass, Japan) and was heated on a hot plate at 120 °C for 15 min. The glass slides were stored at room temperature until further use. Just before use, 80 μL of Milli-Q water was placed on the coated side of the coverglass and left for 10 min to swell the polymer brush. After removing water by blowing air, double-sided tape with a φ13 mm hole (thickness 160 μm, Nitto Denko No.5000NS, Japan) was attached as a spacer. A four-microliter aliquot of DNA solution was applied to the center of the opening, a non-coated coverslip was placed on top, and the sample was incubated on a 37 °C hot plate. During incubation, the samples were observed using a confocal laser scanning microscope (LSM-700, Carl Zeiss) with a water-immersion 40× lens (C-Apochromat 40×/1.2 w CorrECS M27).

Preparation and observation of monodisperse GVs containing DNA condensates

The microfluidic channel for producing monodisperse GVs was fabricated using a standard one-step replica molding process, as described in our previous studies.[45,46] In addition to the DNA solution (internal aqueous phase) prepared as described previously, two additional solutions (external aqueous and oil phases) were prepared (Table S3). The external aqueous phase comprised glucose (500 mM), NaCl (175 mM), Tris-HCl (pH 8.0, 20 mM), pluronic F-68 (1% v/v), and PVA (0.5% w/v). The oil phase consisted of a mixture of squalene (Wako, Japan) and 1-octanol (Wako, Japan) at a volume ratio of 8 : 2 with EggPC dissolved in chloroform to a final concentration of 6 mg mL^{-1}. To visualize the oil phase and lipid membrane under a fluorescence microscope, rhodamine-DHPE was added at a concentration of 2 μg mL^{-1}. The oil phase was stirred at room temperature (20–25 °C) using a vortex mixer to disperse the lipids.

These three phases were introduced into the microfluidic device using a three-channel pneumatic pump (Droplet generator, Onchip Biotechnologies Inc., Japan) to generate water-in-oil-in-water (W/O/W) droplets. These droplets, having a thin oil shell (1–2 μm) stabilized by the lipid interface, were generated at a frequency of ~7 droplets per second. The W/O/W droplet-containing solution was collected in a test tube *via* tubing connected to a channel outlet. Owing to the buoyancy of the W/O/W droplets in the oil phase, the 5 μL solution containing W/O/W droplets was collected from the upper layer of the test tube using a pipette. The samples were then sandwiched between two coverslips using a double-sided adhesive tape spacer, as in the bulk experiment. As the W/O/W droplets floated to the upper side of the glass slide, the upper coverslip was passivated with 2.5% w/v PVA to prevent oil from spreading. The passivation procedure was the same as that described previously. To maintain a constant environmental temperature, the sample was placed on a 37 °C hot plate and subjected to microscopic observation using a confocal laser scanning microscope.

Results and discussion

Behavior of the immiscible DNA condensates in bulk

In this study, we followed our previous research and adopted a system in which three 40 bp ssDNA oligomers form a Y-motif.[21,44] Through sequence design, three types of ssDNA bind together, leaving a 6 nt-palindromic SE at the terminus (5′-CTCGAG-3′) to construct a three-arm Y-motif (Y_A, Fig. 1a). Additionally, we prepared an orthogonal Y-motif (Y_B, Fig. 1a) with different SE sequences (5′-GCTAGC-3′) to form a condensate that was immiscible with the Y_A condensate. Each motif was fluorescently labeled by adding dye-modified DNA (Cy5 for Y_A and FAM for Y_B). Furthermore, we prepared a six-branched DNA nanostructure (S-motif, Fig. 1a) consisting of six ssDNA strands with three 6 nt SEs corresponding to the SEs of both Y_A and Y_B.

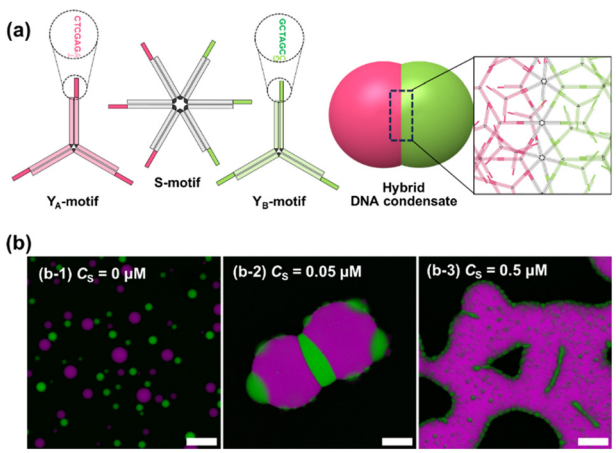

Fig. 1 (a) Schematic representation of two orthogonal Y-motifs (Y_A and Y_B), a linker motif (S-motif), and a hybrid DNA condensate comprised of these three DNA nanostructures. (b) Fluorescent confocal microscope images of DNA condensates composed Y_A and Y_B (5 μM each) supplemented with S-motif at different concentrations in the bulk environment (magenta: Y_A and green: Y_B). All scale bars represent 50 μm.

The Y_A and Y_B motifs hybridize through base-pair interactions with only the like-ones because of the complementary SE sequences, forming distinct condensates. When a small amount of the S-motif is added to a mixture of these two orthogonal Y-motifs, the originally immiscible DNA condensates interacted with each other, as schematically shown on the right side of Fig. 1(a). Herein, the S-motif, which carries both SEs, forms a crossbridge between the two condensates, connecting them to form hybrid condensates. Previous research has shown that by varying the concentration ratio of an S-motif to two Y-motifs, the extent of interaction can be controlled; two condensates can be fully mixed or partially attached.[21]

In this study, we first examined how the macroscopic structure of the two types of orthogonal DNA condensates changed in the bulk condition when the concentration ratio of S-motif to Y-motif was varied. Fluorescence microscope images taken after incubating the mixtures at 37 °C for 24 h with 0, 0.05, and 0.5 μM of S-motif, relative to a concentration of 5 μM for each Y-motif, are shown in Fig. 1(b). Here, we previously confirmed that the oligomers used here form correct Y-motif structures even at room temperature and these Y-motifs with 6 nt SE condensate into the fluidic phase (DNA droplet),[44] so the macroscopic structures appearing after 24 h can be considered to be in thermodynamically equilibrated states.

In the absence of S-motif (C_S = 0 μM), the DNA condensates derived from the Y_A (magenta) and Y_B (green) remained completely separated, with independent polydisperse droplets ranging from 1 to 25 μm in diameter (Fig. 1b, left). Macroscopically, polydisperse spherical condensates were evenly distributed throughout the sample (Fig. S1a). When Brownian motion caused contact between the condensates, fusion was observed between droplets composed of the same motif but not between droplets composed of different motifs. Time-lapse imaging performed every 4 h showed that coalescence almost completely ceased after approximately 4 h, resulting in a relatively stable size distribution (Fig. S2a).

Next, under the condition at C_S = 0.05 μM, characteristic structures were obtained in which Y_A and Y_B condensates were adjacent and attached (Fig. 1b, center). Additionally, the size of the condensates was significantly larger than that in the condition without S-motif, exceeding 100 μm. Despite having the same total amount of the two Y-motifs, only a small number of large condensates were observed in the entire sample (Fig. S1b). This suggests that the presence of the S-motif facilitates the interaction between two motifs to practically doubled the concentration, promoting their coalescence more than when the two Y-motifs existed without interaction. In terms of morphology, the large Y_A condensates were surrounded by relatively smaller Y_B condensates. Confocal images of each fluorescent signal revealed that the

positions of Y_A and Y_B were clearly separated under all S-motif concentrations (Fig. S3).

Furthermore, with C_S = 0.5 μM, even larger and irregularly shaped condensates appeared. The largest proportion of these condensates were composed of Y_A condensates, with fine Y_B condensates adsorbed both inside and on the periphery. From a macroscopic perspective (Fig. S1 and S2), irregular condensates were sparsely formed throughout the sample during the early stages of observation (4 h). Over time, the condensates gradually fused in a manner similar to percolation, and by 24 h, only a few extremely large condensates (>1 mm) were distributed across the sample at random locations.

These results indicate that the ratio of the S-motif to Y-motif, in addition to the total concentration, determines the final size and shape of complex DNA condensates. As the concentration of the S-motif increases, the interaction between the two orthogonal Y-motifs becomes stronger, making it more difficult to predict or control the final size and shape of the condensates. Additionally, under all the conditions tested above, despite both types of Y-motifs being present at the same concentration, the Y_A motifs formed larger condensates. As a representative example, in the condition with C_S = 0 μM, the total volume of each condensate within the 1.28 mm × 1.28 mm field of view (1.4 pL in volume) was estimated to be 2.2 nL for Y_A and 0.56 nL for Y_B, showing nearly a four-fold difference. For individual droplets, the volume of Y_A was 4.8 times greater than that of Y_B (Fig. S4).

This indicated that the Y_A condensate could have a greater binding enthalpy than the Y_B condensate, although the contribution of kinetic aspects cannot be excluded.[47] This hypothesis was supported by the lower fluidity observed for the Y_A condensate, as revealed by the fluorescence recovery after the photobleaching experiment (Fig. S5). The binding free energies of the two SE sequences for each motif were calculated using the web-based NUPACK software. Although the GC-contents were set to be the same, the estimated results showed that the binding free energy of the Y_A-SE (5′-CTCGAG-3′) was −8.03 kcal mol^{-1}, while that of the Y_B-SE (5′-GCTAGC-3′) was −8.31 kcal mol^{-1}, at 175 mM NaCl and 25 °C. Thus, this estimation does not explain the observation that the Y_A-motif condensation grew larger and was more stable. Significant differences in physical properties among nanostar condensates with similar sequences were also reported in the previous study.[48] It is possible that, in addition to the effect of SE sequences, the terminal end stacking, as well as the nearest neighbor stacking, could be responsible for the variation in the melting temperature.[49] Although we cannot fully explain the reason for this discrepancy between the two Y-motifs, we suppose that even slight differences in the sequences of each motif can influence the final size and formation dynamics of the condensates. Consequently, the Y_A condensates appeared earlier than Y_B, grew faster, and remained larger, owing to the greater equilibrium constant.

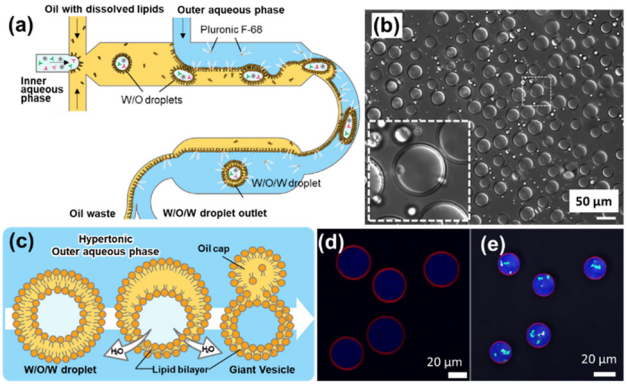

Fig. 2 (a) Schematic illustration of the microfluidic device used to produce monodisperse GVs. (b) Bright-field image of W/O/W droplets produced using the microfluidic device. (c) Schematic illustration of GV shrinkage induced by osmotic action. (d and e) Fluorescent confocal images of W/O/W droplets (d) immediately after collection from the microfluidic device and (e) those at 30 min after collection (blue: internal volume marker, red: membrane marker, magenta and green: Y_A and Y_B condensate).

This trend led to the formation of a Y_A condensates as major structures to which smaller Y_B condensates were attached.

Preparation of uniform GVs containing Y-motifs

We used a microfluidic channel developed in our previous study[45,46] to encapsulate two types of Y-motifs, each at an initial concentration of 1 μM, with varying concentrations of S-motif and 35 mM NaCl into lipid-stabilized thin-shelled W/O/W droplets. No DNA condensates were formed under these concentration conditions.[44] Fig. 2(a) presents a schematic illustration of W/O/W droplet formation in the microfluidic channel. Initially, W/O droplets encapsulating the Y-motif solution surrounded by lipids were generated using hydrodynamic flow focusing. Subsequently, the outer aqueous phase was introduced downstream, causing the W/O droplets to press against the O–W interface. At the bent section of the channel, the W/O droplets crossed the O–W interface, forming W/O/W droplets. The solution discharged from the channel outlet was collected, and many uniform W/O/W droplets were obtained upon microscopic observation (Fig. 2b). At this stage, a thin oil layer covered the inner solution, giving the droplets a double-contoured appearance (Fig. 2b, enlarged view).

In this system, the external environment was changed to hypertonic after the formation of W/O/W droplets, causing the GVs to shrink and increasing the concentration of the encapsulated molecules (Fig. 2c). During this process, oil dewetting led to the formation of lipid bilayer vesicles with attached oil caps. The extent of shrinkage is controlled by the concentration of membrane-impermeable molecules such as sugars and ions. In this study, the concentration of the abundant small molecules (glucose, NaCl, and Tris buffer) in the outer aqueous

phase was adjusted to five times that in the inner water phase. Specifically, the initial GV volume before shrinkage, denoted as V_0, and the GV volume after 30 min of shrinkage, denoted as V, were adjusted such that the shrinkage ratio, V/V_0, was 0.2.

Fig. 2(d) shows the fluorescent confocal microscopy images of the W/O/W droplets immediately after collection and the GVs that shrank owing to osmotic action following dewetting. The W/O/W droplets immediately after collection have a diameter of 35.2 ± 1.8 μm (the number following ± represents the standard deviation of n = 5 images; Fig. 2d), with a relatively thick membrane layer (~1.5 μm) stained in red. The dewetting process began approximately 5 min after the beginning of the observation and occurred stochastically among the individual GVs, with all transitions completed within approximately 30 min. At this stage, the diameter of the internal lumen of GVs was 22.7 ± 0.8 μm because of the osmotic shrinkage (Fig. 2e). The vesicle volume was estimated to be reduced to become 27% of the initial volume at the beginning of the observation. Previously, we confirmed that the extent of osmotic shrinkage of GV is nearly proportional to the osmolarity difference of the solution.[44] Possible reasons why the post-shrinkage volume was larger than the designed 20% is that the assumption of a spherical shape may not be appropriate for all individual GVs, and some extent of shrinkage might have occurred between the W/O/W droplet formation and the observation, even before dewetting. In this study, we proceeded with the following discussion under the assumption that shrinkage induced a five-fold increase in the concentration of encapsulated impermeable molecules. As the concentrations of DNA and NaCl in the internal solution increased, the DNA began to condense.

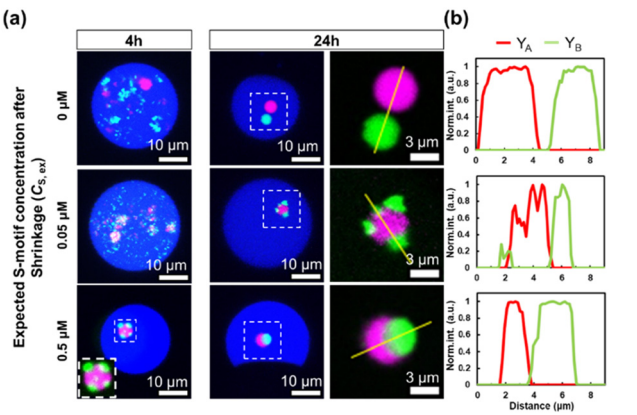

Fig. 3 (a) Confocal microscope images of the Janus-type DNA condensates formed inside GUVs, along with their enlarged views. GUV images at 4 h and 24 h are not identical, but represent majority at each condition and time. Blue indicates the inner aqueous phase of the GUV, magenta represents the Y_A DNA condensates, and green represents the Y_B DNA condensates. (b) Fluorescence intensity profiles of the DNA condensates along the yellow dotted lines drawn on the enlarged view of the DNA condensates.

Formation of immiscible DNA condensates within GVs

As the GVs shrank, the concentrations of DNA and NaCl in the internal solution increased, promoting the complementary binding of SEs in the Y-motif and S-motif, leading to the formation of DNA condensates. Fig. 3(a) shows a close-up view of the typical vesicles, clearly visualizing the state of the DNA condensates formed inside the GVs at 4 and 24 h after being produced in the microfluidic device.

At 4 h after the start of the observation, when the expected concentration of the S-motif ($C_{S,ex}$) after shrinkage was small (0 or 0.05 μM), the emergence of tiny condensates was observed even after 4 h. When focusing on each fluorescence, the DNA condensates from the Y_A-motif (magenta) were relatively large but few in number. In contrast, the DNA condensates from the Y_B-motif (green) were smaller, approximately a few micrometers in size, more abundant, and dispersed throughout the entire internal volume of the GV. Particularly at $C_{S,ex}$ = 0.05 μM, the smaller Y_B-motif condensates adhered around the relatively larger Y_A condensates. At $C_{S,ex}$ = 0.5 μM, no fine and dispersed condensates were observed after 4 h, as the Y_A and Y_B condensates had merged into a single structure within the GV. Similar to the case when $C_{S,ex}$ = 0.05 μM, multiple small Y_B condensates adhered around a large Y_A condensate, forming a single large condensate with a patchy appearance. These results, in conjunction with the bulk experiment, suggested that the higher the concentration of the S-motif, the shorter the time required for the condensates to become a single hybrid blob within the GV. This indicated that the Y_A-motif tended to appear earlier and to form larger condensates than the Y_B-motif condensates. As discussed previously, the ease of DNA condensate formation is likely because of the differences in the free energy of complementary binding between the SE sequences of each motif.

At 24 h, no small, dispersed DNA condensates were observed at any concentration of the S-motif; instead, only a single or a few condensates of each motif were formed (Fig. 3a). This result suggests that over time, smaller condensates of the same type fuse together within the GVs. When C_S = 0 μM, similar to the results in Fig. 1(b), condensates of Y_A-motif and Y_B-motif were spatially segregated. In contrast, when $C_{S,ex}$ = 0.05 μM, a patchy structure was observed where multiple Y_B-motif condensates adhered around a single and larger Y_A-motif condensate. Furthermore, at $C_{S,ex}$ = 0.5 μM, a Janus-type structure was formed where two single DNA condensates of nearly the same size were adjacent, sharing a common interface. For each S-motif concentration, the line profiles of the fluorescence intensity (along the yellow lines) from the fluorescence images of the DNA condensates were plotted (Fig. 3b). The locations of the high-intensity red and green fluorescence signals differed in the condensates formed at each S-motif concentration. Additionally, when the S-motif was present, the condensates of both motifs were adjacent to each other.

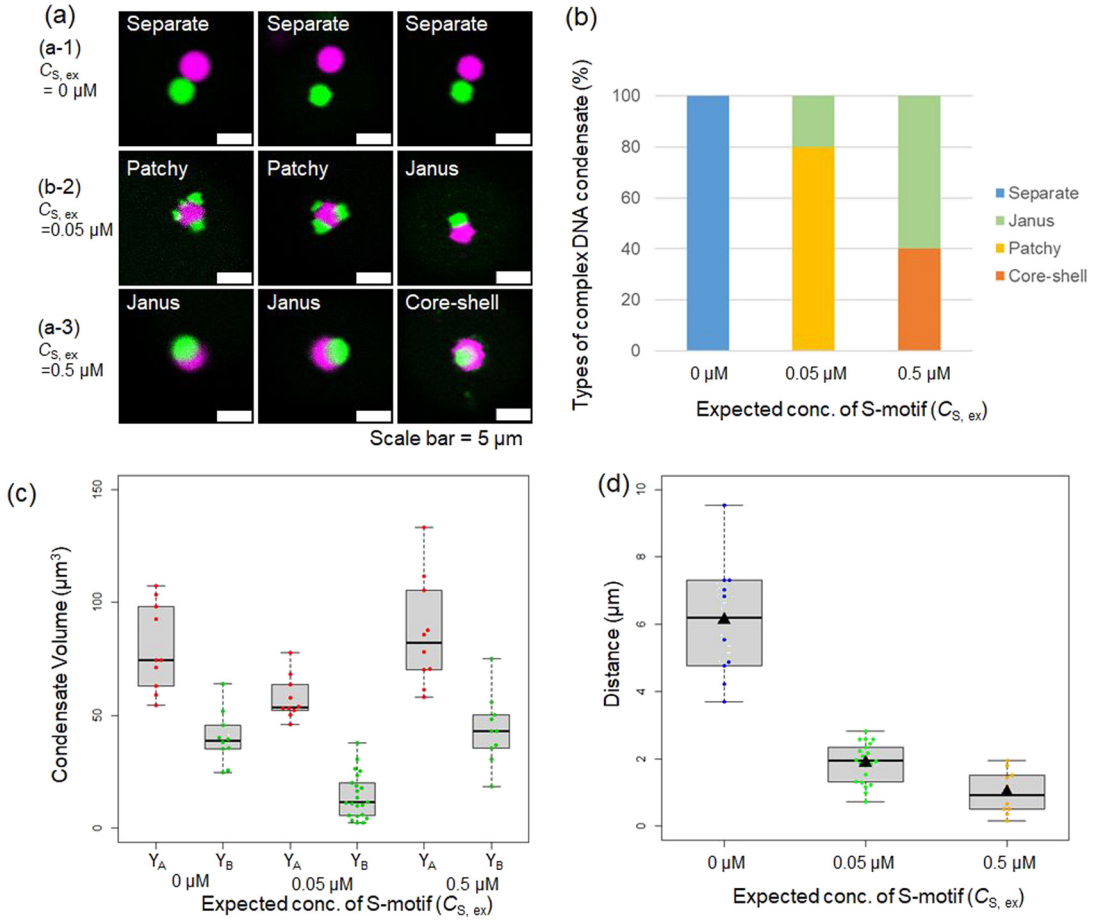

Fig. 4 Detailed analysis of hybrid DNA condensates generated within uniform GVs at different S-motif concentrations. (a) Typical example images of hybrid DNA condensates. (b) Ratios of morphologies of hybrid condensates at each S-motif concentration. (c) Beeswarm and box plots of the volume of Y_A and Y_B condensates estimated from the *z*-stacks of fluorescent confocal image slices. (d) Beeswarm and box plot of the distance between the 3D centers of intensity, characterizing the distance between Y_A and Y_B condensates.

In this experimental system, we took advantage of the uniformity of the GV population and performed a morphological analysis of the condensates within 10 randomly selected GVs under each condition. Representative images (three per condition) are shown in Fig. 4(a) (all images used for the statistics are shown in Fig. S6). The proportions of the different condensate morphologies observed among the 10 GVs under each condition are summarized in Fig. 4(b). Under the condition of $C_{S,ex}$ = 0 μM (Fig. 4a-1), independent single condensates of Y_A and Y_B of comparable sizes were observed in each vesicle. Although the encapsulated concentrations of Y_A and Y_B were equal, similar to the results observed in the bulk experiment (Fig. 1a), the condensates of Y_A were slightly larger. At $C_{S,ex}$ = 0.05 μM (Fig. 4a-2), in 80% of the GVs, a "patchy structure" was observed, where two or more small Y_B condensates adhered around a relatively large single Y_A condensate. In the remaining 20% of GVs, a "Janus structure" was observed, where one Y_A and one Y_B condensate were adhered next to each other. At $C_{S,ex}$ = 0.5 μM (Fig. 4a-3), the proportion of Janus structures increased to 60%, and the remainder showed a "core–shell structure", where a Y_B condensate core was surrounded by a Y_A condensate shell.

Next, we calculated the volume of each condensate from confocal slice images taken at 1 μm intervals and created a bee swarm plot as shown in Fig. 4(c) (the same population of 10 GVs as in Fig. 4(b) was used. Numbers following ± represents the standard deviation). First, under all linker concentration conditions, each GV contained one Y_A condensate, with volumes of 80 ± 18 μm^3, 58 ± 9 μm^3, and 86 ± 23 μm^3 at $C_{S,ex}$ = 0, 0.05, and 0.5 μM, respectively (overall 74 ± 21 μm^3). Assuming a spherical shape, this corresponds to a diameter of approximately 4.7–5.7 μm. Considering the measurement errors owing to condensate movement during *z*-slice acquisition, these condensates were fairly uniform. However, the size and number of the Y_B condensates varied depending on the S-motif concentration. At $C_{S,ex}$ = 0 μM, one Y_B condensate per GV was present, with a volume of 40 ± 11 μm^3, approximately 50% of the Y_A condensate volume. This was larger than the total volume ratio of Y_A to Y_B observed in the bulk experiments ($V_{YB,total}/V_{YA,total}$ ~20%; Fig. S4 in the SI). Although the reason for this discrepancy is unclear, it suggests that the volume of DNA condensates is highly

sensitive to slight differences in the binding enthalpy or environmental factors, even when the sequences are macroscopically homogeneous. Similarly, at $C_{S,ex}$ = 0.5 μM, one Y_B condensate per GV was present, with a comparable volume of 44 ± 15 μm^3. However, the condensate morphology under these conditions exhibited Janus or core–shell structures. We measured the three-dimensional distance between the centers of mass of Y_A and Y_B condensates (Fig. 4d) and found it to be 6.1 ± 1.7 μm at $C_{S,ex}$ = 0 μM and 1.0 ± 0.6 μm at $C_{S,ex}$ = 0.5 μM, respectively. The former distance is of the order of the characteristic length of the GV after shrinkage, whereas the latter is of the order of the condensate size (in core–shell structures, the centers of mass coincide). Finally, at $C_{S,ex}$ = 0.05 μM, around one Y_A condensate (58 ± 9 μm^3 in volume), 2–4 smaller Y_B condensates were attached. Reflecting this morphology, the average volume of the Y_B condensates was 14 ± 10 μm^3. The distance between the center of mass of the Y_A condensate and each small Y_B condensate was 1.9 ± 0.6 μm, again on the characteristic length scale of the condensates.

In summary, these results demonstrate that the formation of condensates within the confined and uniform microenvironment of GVs promotes collisions between fine condensates under limited DNA concentrations, resulting in hybrid DNA condensates with good reproducibility in both size and morphology.

Conclusion

In this study, we demonstrated that uniform hybrid DNA condensates, composed of two types of orthogonal DNA Y-motifs and a linker DNA motif, can be generated with uniform size and structure inside monodisperse GVs using a microfluidic device. By employing the volume modulation of GVs induced by osmotic action, we demonstrated that specific morphologies such as patchy and Janus-type condensates could be reproducibly formed from a defined amount of DNA enclosed in uniform GVs, depending on the concentration of the linker motif. A similar molecular concentration operation within a uniform microcompartment can be achieved using uniform water-in-oil droplets, where water diffuses into the oil phase.[50,51] However, the precise control of the degree of shrinkage requires methods to tune the partition coefficient of water into oil, which is likely to be challenging. A major advantage of using GVs is that the osmotic pressure between the external and internal solutions can be easily manipulated, making it easier to control the concentration rates. Furthermore, the fact that the compartments are composed of lipid bilayers presents a significant benefit for the future development of more advanced artificial cells, *e.g.*, with integrated membrane proteins.

In summary, this study serves as a foundational model for controlling the spatial relationships and interactions of phase-separated droplets to construct hierarchical artificial cells using liquid–liquid phase separation systems. Applications of this system could include, for example, molecular detection within artificial cells,[35,42,52] as mentioned in the introduction, or the control of gene expression from complex DNA droplets containing multiple types of genes.[53] Our microfluidic system holds great potential as a reproducible and user-friendly platform for constructing such artificial cell systems.

Author contributions

R. Y. designed conducted all experiments. R. U. established the microfluidic formation of monodisperse GV to encapsulate DNA Y-motifs. R. S. and M. T. prepared the SE-modified gene and helped with molecular biology experiments. T. M. and M. T. supervised the experimental design of DNA condensates. H. S. directed and supervised the entire project, and R. Y. and H. S. wrote the manuscript.

Conflicts of interest

There are no conflicts of interest to declare.

Data availability

Supplementary information is available: Fig. S1 Tile-scanned images of orthogonal DNA condensates with a linker S-motif at different concentrations. Fig. S2 Time sequence of the orthogonal DNA condensates in the bulk solution. Fig. S3 Merged and separated fluorescent images of each DNA condensate at different linker motif concentrations. Fig. S4 Size distributions of YA and YB (5 μM each) droplets without linker. Fig. S5 Results of the fluorescent recovery after photobleaching (FRAP) experiment. Fig. S6 Fluorescent confocal laser scanning microscope images used for the statistical analysis. Table S1. Sequences of DNA oligomers. Table S2. Compositions of the condensate formation tests in bulk condition. Table S3. Compositions of the three solutions used for GV production. See DOI: **https://doi.org/10.1039/D5LF00131E**.

The data supporting the findings of this study are available from the corresponding author upon reasonable request.

Acknowledgements

This study was supported by JSPS Grants 19H02576, 19H00901, 20H05935, 24K01320, and 24H01155 and the Institute of Science and Engineering at Chuo University. We thank Mr. Zhitai Huang in our group for performing additional experiments.

Notes and references

1 J. Z. Du and R. K. O'Reilly, *Chem. Soc. Rev.*, 2011, **40**, 2402–2416.
2 J. Hu, S. Zhou, Y. Sun, X. Fang and L. Wu, *Chem. Soc. Rev.*, 2012, **41**, 4356–4378.
3 S. Jiang, Q. Chen, M. Tripathy, E. Luijten, K. S. Schweizer and S. Granick, *Adv. Mater.*, 2010, **22**, 1060–1071.
4 A. B. Pawar and I. Kretzschmar, *Macromol. Rapid Commun.*, 2010, **31**, 150–168.

5 F. I. Seyni and B. P. Grady, *Colloid Polym. Sci.*, 2021, **299**, 585–593.
6 A. Walther and A. H. E. Muller, *Soft Matter*, 2008, **4**, 663–668.
7 Z. He and I. Kretzschmar, *Langmuir*, 2012, **28**, 9915–9919.
8 M. D. McConnell, M. J. Kraeutler, S. Yang and R. J. Composto, *Nano Lett.*, 2010, **10**, 603–609.
9 S. Seiffert, M. B. Romanowsky and D. A. Weitz, *Langmuir*, 2010, **26**, 14842–14847.
10 K. Maeda, H. Onoe, M. Takinoue and S. Takeuchi, *Adv. Mater.*, 2012, **24**, 1340–1346.
11 S. Ghosh and P. Schurtenberger, *Colloids Surf., A*, 2019, **573**, 205–210.
12 M. Hayakawa, H. Onoe, K. H. Nagai and M. Takinoue, *Sci. Rep.*, 2016, **6**, 20793.
13 E. Lattuada, M. Leo, D. Caprara, L. Salvatori, A. Stoppacciaro, F. Sciortino and P. Filetici, *Front. Pharmacol.*, 2020, **11**, 01345.
14 Y. H. Dong, C. Yao, Y. Zhu, L. Yang, D. Luo and D. Y. Yang, *Chem. Rev.*, 2020, **120**, 9420–9481.
15 D. Wang, P. F. Liu and D. Luo, *Angew. Chem., Int. Ed.*, 2022, 61.
16 H. Udono, J. Gong, Y. Sato and M. Takinoue, *Adv. Biol.*, 2023, **7**, e2200180.
17 M. Takinoue, *Interface Focus*, 2023, **13**, 20230021.
18 S. Biffi, R. Cerbino, F. Bomboi, E. M. Paraboschi, R. Asselta, F. Sciortino and T. Bellini, *Proc. Natl. Acad. Sci. U. S. A.*, 2013, **110**, 15633–15637.
19 N. Conrad, T. Kennedy, D. K. Fygenson and O. A. Saleh, *Proc. Natl. Acad. Sci. U. S. A.*, 2019, **116**, 7238–7243.
20 D. T. Nguyen, B. J. Jeon, G. R. Abraham and O. A. Saleh, *Langmuir*, 2019, **35**, 14849–14854.
21 Y. Sato, T. Sakamoto and M. Takinoue, *Sci. Adv.*, 2020, 6.
22 S. Agarwal, D. Osmanovic, M. A. Klocke and E. Franco, *ACS Nano*, 2022, **16**, 11842–11851.
23 T. Lee, S. Do, J. G. Lee, D. N. Kim and Y. Shin, *Nanoscale*, 2021, **13**, 17638–17647.
24 M. Du and Z. J. Chen, *Science*, 2018, **361**, 704–709.
25 M. A. Boyd and N. P. Kamat, *Trends Biotechnol.*, 2021, **39**, 927–939.
26 J. Bucci, L. Malouf, D. A. Tanase, N. Farag, J. R. Lamb, R. Rubio-Sanchez, S. Gentile, E. Del Grosso, C. F. Kaminski, L. Di Michele and F. Ricci, *J. Am. Chem. Soc.*, 2024, **146**, 31529–31537.
27 K. Jeon, C. Lee, J. Y. Lee and D. N. Kim, *ACS Appl. Mater. Interfaces*, 2024, **16**, 24162–24171.
28 S. Agarwal, D. Osmanovic, M. Dizani, M. A. Klocke and E. Franco, *Nat. Commun.*, 2024, **15**, 1915.
29 N. Park, J. S. Kahn, E. J. Rice, M. R. Hartman, H. Funabashi, J. F. Xu, S. H. Um and D. Luo, *Nat. Protoc.*, 2009, **4**, 1759–1770.
30 N. Park, S. H. Um, H. Funabashi, J. F. Xu and D. Luo, *Nat. Mater.*, 2009, **8**, 432–437.
31 A. A. Zinchenko, H. Sakai, S. Matsuoka and S. Murata, *J. Hazard. Mater.*, 2009, **168**, 38–43.
32 S. Do, C. Lee, T. Lee, D. N. Kim and Y. Shin, *Sci. Adv.*, 2022, **8**, eabj1771.
33 M. Dizani, D. Sorrentino, S. Agarwal, J. M. Stewart and E. Franco, *J. Am. Chem. Soc.*, 2024, **146**, 29344–29354.
34 A. Leathers, M. Walczak, R. A. Brady, A. Al Samad, J. Kotar, M. J. Booth, P. Cicuta and L. Di Michele, *J. Am. Chem. Soc.*, 2022, **144**, 17468–17476.
35 J. Gong, N. Tsumura, Y. Sato and M. Takinoue, *Adv. Funct. Mater.*, 2022, **32**, 2202322.
36 S. Agarwal, M. Dizani, D. Osmanovic and E. Franco, *Interface Focus*, 2023, **13**, 20230017.
37 Y. Sato and M. Takinoue, *Biophys. Physicobiol.*, 2024, **21**, e210010.
38 J. M. Stewart, S. Li, A. A. Tang, M. A. Klocke, M. V. Gobry, G. Fabrini, L. Di Michele, P. W. K. Rothemund and E. Franco, *Nat. Commun.*, 2024, **15**, 6244.
39 B. J. Jeon, D. T. Nguyen and O. A. Saleh, *J. Phys. Chem. B*, 2020, **124**, 8888–8895.
40 M. Walczak, R. A. Brady, L. Mancini, C. Contini, R. Rubio-Sanchez, W. T. Kaufhold, P. Cicuta and L. Di Michele, *Nat. Commun.*, 2021, **12**, 4743.
41 M. P. Tran, R. Chatterjee, Y. Dreher, J. Fichtler, K. Jahnke, L. Hilbert, V. Zaburdaev and K. Gopfrich, *Small*, 2023, **19**, e2202711.
42 T. Maruyama, J. Gong and M. Takinoue, *Nat. Commun.*, 2024, **15**, 7397.
43 H. Udono, M. Fan, Y. Saito, H. Ohno, S. M. Nomura, Y. Shimizu, H. Saito and M. Takinoue, *ACS Nano*, 2024, **18**, 15477–15486.
44 R. Yoneyama, N. Morikawa, R. Ushiyama, T. Maruyama, R. Sato, M. Tsugane, M. Takinoue and H. Suzuki, *JACS Au*, 2025, **5**, 3533–3544.
45 R. Ushiyama, K. Koiwai and H. Suzuki, *Sens. Actuators, B*, 2022, **355**, 131281.
46 R. Ushiyama, S. Nanjo, M. Tsugane, R. Sato, T. Matsuura and H. Suzuki, *ACS Synth. Biol.*, 2023, **13**, 68–76.
47 S. Agarwal, D. Osmanovic, M. A. Klocke and E. Franco, *ACS Nano*, 2022, **16**, 11842–11851.
48 Y. Sato and M. Takinoue, *Nanoscale Adv.*, 2023, **5**, 1919.
49 J. A. Punnoose, D. Cole, T. Melfi, V. Morya, B. R. Madhanagopal, A. A. Chen, S. Vangaveti, A. R. Chandrasekaran and K. Halvorsen, *bioRxiv*, 2024, preprint, DOI: **10.1101/2024.06.10.598265**.
50 E. Sokolova, E. Spruijt, M. M. K. Hansen, E. Dubuc, J. Groen, V. Chokkalingam, A. Piruska, H. A. Heus and W. T. S. Huck, *Proc. Natl. Acad. Sci. U. S. A.*, 2013, **110**, 11692–11697.
51 T. Wu, K. Hirata, H. Suzuki, R. Xiang, Z. Tang and T. Yomo, *Appl. Phys. Lett.*, 2012, **101**, 074108.
52 M. Tsugane and H. Suzuki, *Sci. Rep.*, 2018, **8**, 9214.
53 K. Nishimura, S. Tsuru, H. Suzuki and T. Yomo, *ACS Synth. Biol.*, 2015, **4**, 566–576.